Barotropic Instability

ABSTRACT

The waves explored in the previous chapter evolve in a fluid otherwise at rest, propagating without either growth or decay. Here, we investigate waves riding on an existing current and find that, under certain conditions, they may grow at the expense of the energy contained in the mean current while respecting conservation of vorticity. The numerical section exposes the method of contour dynamics, designed specifically for applications in which conservation of vorticity is important.

10.1 WHAT MAKES A WAVE GROW UNSTABLE?

The planetary and topographic waves described in the previous chapter (Sections 9.4 through 9.5) owe their existence to the presence of an ambient potential-vorticity gradient. In the case of planetary waves, the cause is the sphericity of the planet, whereas for topographic waves the gradient results from the bottom slope. We may naturally wonder whether a sheared current that possesses a gradient of relative vorticity, would, too, be able to sustain similar low-frequency waves.

However, the situation is quite different for several reasons. First, the current would not only create the required ambient potential-vorticity gradient but would also transport the wave pattern; because of the current shear, this translation would be differential, and the wave pattern would be rapidly distorted. Moreover, there is likely to be a place within the current where the speed of the wave matches the velocity of the current; such a location, termed a *critical level*, typically permits a vigorous transfer of energy between the current and the wave. As a consequence, the wave may draw energy from the current and grow in time. If this happens, insignificant little wiggles may turn into very large perturbations, and the initial flow can become highly contorted, to the point of becoming unrecognizable. The flow is said to be unstable. To distinguish this situation from other instabilities occurring in baroclinic fluids (i.e., those possessing a stratification; see Chapters 14 and 17), the preceding process is generally known as *barotropic instability*.

The stability theory of homogeneous shear flows is a well-developed chapter in fluid mechanics (see, e.g., Kundu, 1990, Section 11.9; Lindzen, 1988). Here,

we address the problem with the inclusion of the Coriolis force but limit our investigation to establishing general properties and solving one particular case.

10.2   WAVES ON A SHEAR FLOW

To investigate the behavior of waves on an existing current in a relatively clear and tractable formalism, it is customary to make the following assumptions: The fluid is homogeneous and inviscid, and the bottom and the surface are flat and horizontal. However, the Coriolis parameter is allowed to vary (i.e., the beta effect is retained). The governing equations are (Section 4.4)

$$\frac{\partial u}{\partial t} + u\frac{\partial u}{\partial x} + v\frac{\partial u}{\partial y} + w\frac{\partial u}{\partial z} - fv = -\frac{1}{\rho_0}\frac{\partial p}{\partial x} \tag{10.1a}$$

$$\frac{\partial v}{\partial t} + u\frac{\partial v}{\partial x} + v\frac{\partial v}{\partial y} + w\frac{\partial v}{\partial z} + fu = -\frac{1}{\rho_0}\frac{\partial p}{\partial y} \tag{10.1b}$$

$$0 = -\frac{\partial p}{\partial z} \tag{10.1c}$$

$$\frac{\partial u}{\partial x} + \frac{\partial v}{\partial y} + \frac{\partial w}{\partial z} = 0, \tag{10.1d}$$

where the Coriolis parameter $f = f_0 + \beta_0 y$ varies with the northward coordinate y (Section 9.4). As demonstrated in Section 7.3, a horizontal flow that is initially uniform in the vertical will, in the absence of vertical friction, remain so at all times. In GFD parlance, this is what is called a *barotropic flow*, and we consider such a case. Consequently, we drop the terms $w\partial u/\partial z$ and $w\partial v/\partial z$ in Eqs. (10.1a) and (10.1b), respectively. According to (10.1d), $\partial w/\partial z$ must be z-independent, too, which implies that w is linear in z. But because the vertical velocity vanishes at both top and bottom, it must be zero everywhere ($w = 0$). The continuity equation reduces to

$$\frac{\partial u}{\partial x} + \frac{\partial v}{\partial y} = 0. \tag{10.2}$$

For the basic state, we choose a zonal current with arbitrary meridional profile: $u = \bar{u}(y)$, $v = 0$. This is an exact solution to the nonlinear equations as long as the pressure distribution, $p = \bar{p}(y)$, satisfies the geostrophic balance

$$(f_0 + \beta_0 y)\,\bar{u}(y) = -\frac{1}{\rho_0}\frac{d\bar{p}}{dy}. \tag{10.3}$$

Next, we add a small perturbation, meant to represent an arbitrary wave of weak amplitude. We write

$$u = \bar{u}(y) + u'(x, y, t) \tag{10.4a}$$

$$v = v'(x, y, t) \tag{10.4b}$$

$$p = \bar{p}(y) + p'(x, y, t), \tag{10.4c}$$

where the perturbations u', v', and p' are taken to be much smaller that the corresponding variables of the basic flow (i.e., u' and v' much less than $\bar{u}$, and p' much less than $\bar{p}$). Substitution in Eqs. (10.1a), (10.1b), and (10.2) and subsequent linearization to take advantage of the smallness of the perturbation yield:

$$\frac{\partial u'}{\partial t} + \bar{u}\,\frac{\partial u'}{\partial x} + v'\,\frac{d\bar{u}}{dy} - (f_0 + \beta_0 y)v' = -\frac{1}{\rho_0}\,\frac{\partial p'}{\partial x} \qquad (10.5a)$$

$$\frac{\partial v'}{\partial t} + \bar{u}\,\frac{\partial v'}{\partial x} + (f_0 + \beta_0 y)u' = -\frac{1}{\rho_0}\,\frac{\partial p'}{\partial y} \qquad (10.5b)$$

$$\frac{\partial u'}{\partial x} + \frac{\partial v'}{\partial y} = 0. \qquad (10.5c)$$

The last equation admits the streamfunction ψ, defined as

$$u' = -\frac{\partial \psi}{\partial y}, \quad v' = +\frac{\partial \psi}{\partial x}. \qquad (10.6)$$

The choice of signs corresponds to a flow along streamlines with the higher streamfunction values on the right.

A cross-differentiation of the momentum equations (10.5a) and (10.5b) and the elimination of the velocity components leads to a single equation for the streamfunction:

$$\left(\frac{\partial}{\partial t} + \bar{u}\,\frac{\partial}{\partial x}\right)\nabla^2 \psi + \left(\beta_0 - \frac{d^2\bar{u}}{dy^2}\right)\frac{\partial \psi}{\partial x} = 0. \qquad (10.7)$$

This equation has coefficients that depend on $\bar{u}$ and, therefore, on the meridional coordinate y only. A sinusoidal wave in the zonal direction is then a solution:

$$\psi(x,\ y,\ t) = \phi(y)e^{i(kx-\omega t)}. \qquad (10.8)$$

Substitution provides the following second-order ordinary differential equation for the amplitude $\phi(y)$:

$$\frac{d^2\phi}{dy^2} - k^2\phi + \frac{\beta_0 - d^2\bar{u}/dy^2}{\bar{u}(y) - c}\,\phi = 0, \qquad (10.9)$$

where $c = \omega/k$ is the zonal speed of propagation. An equation of this type is called a *Rayleigh equation* (Rayleigh, 1880). Its key features are the nonconstant coefficient in the third term and the fact that its denominator may be zero, creating a singularity.

For boundary conditions, let us assume for simplicity that the fluid is contained between two walls, at $y = 0$ and L. We are thus considering waves on a zonal flow in a zonal channel. Obviously, there is no such zonal channel in either the atmosphere or ocean, but wavy zonal flows of limited meridional extent abound. The atmospheric jet stream in the upper troposphere, the Gulf Stream after its seaward turn off Cape Hatteras (36°N), and the Antarctic Circumpolar Current are all good examples. Also, the atmosphere on Jupiter, with

the exception of the Great Red Spot and other vortices, consists almost entirely of zonal bands of alternating winds, called *belts* or *stripes* (see Fig. 1.5).

If the boundaries prevent fluid from entering and leaving the channel, v' is zero there, and Eq. (10.6) implies that the streamfunction must be a constant along each wall. In other words, walls are streamlines. This is possible only if the wave amplitude obeys

$$\phi(y=0)=\phi(y=L)=0. \tag{10.10}$$

The second-order, homogeneous problem of Eqs. (10.9) and (10.10) can be viewed as an eigenvalue problem: The solution is trivial ($\phi=0$), unless the phase velocity assumes a specific value (eigenvalue), in which case a nonzero function ϕ (eigenfunction) can be determined within an arbitrary multiplicative constant.

In general, the eigenvalues c may be complex. If c admits the function ϕ, then the complex conjugate c^* admits the complex conjugate function ϕ^* and is thus another eigenvalue. This can be readily verified by taking the complex conjugate of Eq. (10.9). Hence, complex eigenvalues come in pairs.

Decomposing the eigenvalue into its real and imaginary components,

$$c=c_r+\mathrm{i}\,c_i, \tag{10.11}$$

we note that the streamfunction ψ has an exponential factor of the form $\exp(kc_it)$, which grows or decays according to the sign of c_i. Because the eigenvalues come in pairs to any decaying mode will correspond a growing mode. Therefore, the presence of a nonzero imaginary part in the phase velocity c automatically guarantees the existence of a growing disturbance and thus the instability of the basic flow. The product kc_i is then called the *growth rate*. Conversely, for the basic flow to be stable, it is necessary that the phase speed c be purely real.

Because mathematical difficulties prevent a general determination of the c values for an arbitrary velocity profile $\bar{u}(y)$ (the analysis is difficult even for idealized but nontrivial profiles), we shall not attempt to solve the problems (10.9)–(10.10) exactly but will instead establish some of its integral properties and, in so doing, reach weaker stability criteria.

When we multiply Eq. (10.9) by ϕ^* and then integrate across the domain, we obtain

$$-\int_0^L \left(\left|\frac{\mathrm{d}\phi}{\mathrm{d}y}\right|^2+k^2|\phi|^2\right)\mathrm{d}y+\int_0^L \frac{\beta_0-\mathrm{d}^2\bar{u}/\mathrm{d}y^2}{\bar{u}-c}|\phi|^2\,\mathrm{d}y=0, \tag{10.12}$$

after an integration by parts. The imaginary part of this expression is

$$c_i\int_0^L \left(\beta_0-\frac{\mathrm{d}^2\bar{u}}{\mathrm{d}y^2}\right)\frac{|\phi|^2}{|\bar{u}-c|^2}\,\mathrm{d}y=0. \tag{10.13}$$

Two cases are possible: Either c_i vanishes or the integral does. If c_i is zero, the basic flow admits no growing disturbance and is stable. But, if c_i is not zero, then the integral must vanish, which requires that the quantity

$$\beta_0 - \frac{d^2\bar{u}}{dy^2} = \frac{d}{dy}\left(f_0 + \beta_0 y - \frac{d\bar{u}}{dy}\right) \tag{10.14}$$

must change sign at least once within the confines of the domain. Summing up, we conclude that a necessary condition for instability is that expression (10.14) vanish somewhere inside the domain. Conversely, a sufficient condition for stability is that expression (10.14) not vanish anywhere within the domain (on the boundaries maybe, but not inside the domain). Physically, the total vorticity of the basic flow, $f_0 + \beta_0 y - d\bar{u}/dy$, must reach an extremum within the domain to cause instabilities. This result was first derived by Kuo (1949).

This first criterion can be strengthened by considering next the real part of Eq. (10.12), which takes the form

$$\int_0^L (\bar{u} - c_r)\left(\beta_0 - \frac{d^2\bar{u}}{dy^2}\right) \frac{|\phi|^2}{|\bar{u} - c|^2}\, dy = \int_0^L \left(\left|\frac{d\phi}{dy}\right|^2 + k^2|\phi|^2\right) dy. \tag{10.15}$$

In the event of instability, the integral in Eq. (10.13) vanishes. Multiplying it by $(c_r - \bar{u}_0)$, where $\bar{u}_0$ is any real constant, adding the result to Eq. (10.15), and noting that the right-hand side of Eq. (10.15) is always positive for nonzero perturbations, we obtain

$$\int_0^L (\bar{u} - \bar{u}_0)\left(\beta_0 - \frac{d^2\bar{u}}{dy^2}\right) \frac{|\phi|^2}{|\bar{u} - c|^2}\, dy > 0. \tag{10.16}$$

This inequality demands that the expression

$$(\bar{u} - \bar{u}_0)\left(\beta_0 - \frac{d^2\bar{u}}{dy^2}\right) \tag{10.17}$$

be positive in at least some finite portion of the domain. Because this must hold true for any constant $\bar{u}_0$, it must be true in particular if $\bar{u}_0$ is the value of $\bar{u}(y)$ where $\beta_0 - d^2\bar{u}/dy^2$ vanishes. Hence, a stronger criterion is: Necessary conditions for instability are that $\beta_0 - d^2\bar{u}/dy^2$ vanish at least once within the domain *and* that $(\bar{u} - \bar{u}_0)(\beta_0 - d^2\bar{u}/dy^2)$, where $\bar{u}_0$ is the value of $\bar{u}(y)$ at which the first expression vanishes, be positive in at least some finite portion of the domain. Although this stronger criterion still offers no sufficient condition for instability, it is generally quite useful.

10.3   BOUNDS ON WAVE SPEEDS AND GROWTH RATES

The preceding analysis taught us that instabilities may occur when certain conditions are met. A question then naturally arises: If the flow is unstable, how fast will perturbations grow? In the general case of an arbitrary shear flow $\bar{u}(y)$, a precise determination of the growth rate of unstable perturbations is not possible. However, an upper bound can be derived relatively easily, and in the process, we can also determine lower and upper bounds on the phase speed of the perturbations. For simplicity, we will restrict our attention to the f-plane ($\beta_0 = 0$), in which case the derivation is due to Howard (1961). Afterwards, we will cite, without demonstration, the result for the beta plane.

The analysis begins by a change of variable[1]:

$$\phi = (\bar{u} - c)\, a, \tag{10.18}$$

which transforms Eq. (10.9) into

$$\frac{\mathrm{d}}{\mathrm{d}y}\left[(\bar{u} - c)^2\, \frac{\mathrm{d}a}{\mathrm{d}y}\right] - k^2\, (\bar{u} - c)^2\, a = 0, \tag{10.19}$$

with β_0 set to zero. Because of Eq. (10.18), the boundary conditions on a are identical to those on ϕ, namely, $a(0) = a(L) = 0$.

We consider the case of an unstable wave. In this case, c has a nonzero imaginary part, and a is nonzero and complex. Multiplying by the complex conjugate a^* and integrating across the domain, we obtain an expression whose real and imaginary parts are

$$\text{Real part:}\quad \int_0^L [(\bar{u} - c_r)^2 - c_i^2]P\, \mathrm{d}y = 0 \tag{10.20}$$

$$\text{Imaginary part:}\quad \int_0^L (\bar{u} - c_r)P\, \mathrm{d}y = 0, \tag{10.21}$$

where $P = |\mathrm{d}a/\mathrm{d}y|^2 + k^2|a|^2$ is a nonzero positive quantity. With Eq. (10.21), Eq. (10.20) can also be recast as

$$\int_0^L [\bar{u}^2 - (c_r^2 + c_i^2)]P\, \mathrm{d}y = 0. \tag{10.22}$$

---

[1] It can be shown that the new variable a is the meridional displacement, the material time derivative of which is the v component of velocity.

It immediately follows from Eq. (10.21) that $(\bar{u} - c_r)$ must vanish somewhere in the domain, implying that the phase speed c_r lies between the minimum and maximum values of $\bar{u}(y)$:

$$U_{\min} \;<\; c_r \;<\; U_{\max}. \tag{10.23}$$

Physically, the wavy perturbation, if unstable, must travel with a speed that matches that of the entraining flow, in at least one location. In other words, there will always be a place in the domain where the wave does not drift with respect to the ambient flow and grows in place. It is precisely this local coupling between wave and flow that allows the wave to extract energy from the flow and to grow at its expense. The location where the phase speed is equal to the flow velocity is called a *critical level*.

Armed with bounds for the real part of c, we now seek bounds on its imaginary part. To do so, we introduce the obvious inequality

$$\int\limits_{0}^{L} (\bar{u} - U_{\min})\,(U_{\max} - \bar{u})P \, \mathrm{d}y \;\geq\; 0 \tag{10.24}$$

and then expand the expression, replace all linear terms in $\bar{u}$ using Eq. (10.21), and replace the quadratic term using Eq. (10.22) to arrive at

$$\left[\left(c_r - \frac{U_{\min} + U_{\max}}{2} \right)^2 + c_i^2 - \left(\frac{U_{\max} - U_{\min}}{2} \right)^2 \right] \int\limits_{0}^{L} P \, \mathrm{d}y \;\leq\; 0. \tag{10.25}$$

Because the integral of P can only be positive, the preceding bracketed quantity must be negative:

$$\left(c_r - \frac{U_{\min} + U_{\max}}{2} \right)^2 + c_i^2 \;\leq\; \left(\frac{U_{\max} - U_{\min}}{2} \right)^2. \tag{10.26}$$

This inequality implies that, in the complex plane, the number $c_r + i c_i$ must lie within the circle centered at $[(U_{\min} + U_{\max})/2, 0]$ and of radius $(U_{\max} - U_{\min})/2$. Since we are interested in modes that grow in time, c_i is positive, and only the upper half of that circle is relevant (Fig. 10.1). This result is called *Howard's semicircle theorem*.

It is readily evident from inequality (10.26) or Fig. 10.1 that c_i is bounded above by

$$c_i \;\leq\; \frac{U_{\max} - U_{\min}}{2}. \tag{10.27}$$

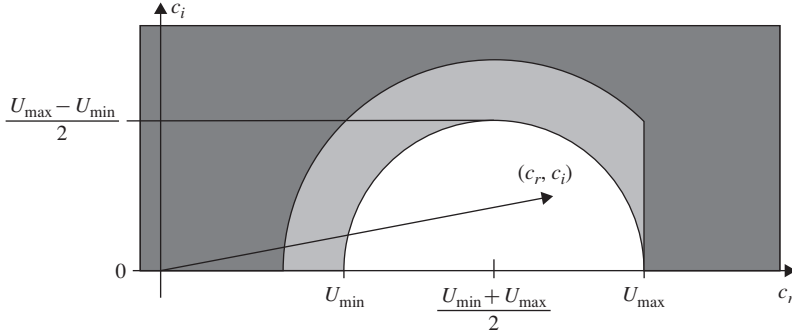The perturbation's growth rate $k c_i$ is thus likewise bounded above.

FIGURE 10.1   The semicircle theorem. Growing perturbations of wavenumber k must have phase speeds c_r and growth rates kc_i such that the tip of the vector (c_r, c_i) falls within the half-circle constructed from the minimum and maximum velocities of the ambient shear flow $\bar{u}(y)$, as depicted in the figure. When the beta effect is taken into account, the tip of the vector must lie in the slightly enlarged domain that includes the semicircle and the light gray area.

On the beta plane, the treatment of integrals and inequalities is somewhat more elaborate but still feasible. Pedlosky (1987, Section 7.5) showed that the preceding inequalities on c_r and c_i must be modified to

$$U_{\min} - \frac{\beta_0 L^2}{2(\pi^2 + k^2 L^2)} \; < \; c_r \; < \; U_{\max} \tag{10.28}$$

$$\left(c_r - \frac{U_{\min} + U_{\max}}{2}\right)^2 + c_i^2 \; \leq \; \left(\frac{U_{\max} - U_{\min}}{2}\right)^2 + \frac{\beta_0 L^2 (U_{\max} - U_{\min})}{2(\pi^2 + k^2 L^2)}, \tag{10.29}$$

where L is the domain's meridional width and k the zonal wavenumber (Fig. 10.1). The westward velocity shift on the left side of Eq. (10.28) is related to the existence of planetary waves [see the zonal phase speed, (9.30)]. The last inequality readily leads to an upper bound for the growth rate kc_i. Knowing bounds for the phase speed c_r and growth rate kc_i is useful in the numerical search of stability threshold in specific applications (Proehl, 1996).

10.4   A SIMPLE EXAMPLE

The preceding considerations on the existence of instabilities and their properties are rather abstract. So, let us work out an example to illustrate the concepts. For simplicity, we restrict ourselves to the f-plane ($\beta_0 = 0$) and take a shear flow that is piecewise linear (Fig. 10.2):

$$y < -L: \quad \bar{u} = -U, \quad \frac{d\bar{u}}{dy} = 0, \quad \frac{d^2\bar{u}}{dy^2} = 0 \tag{10.30}$$
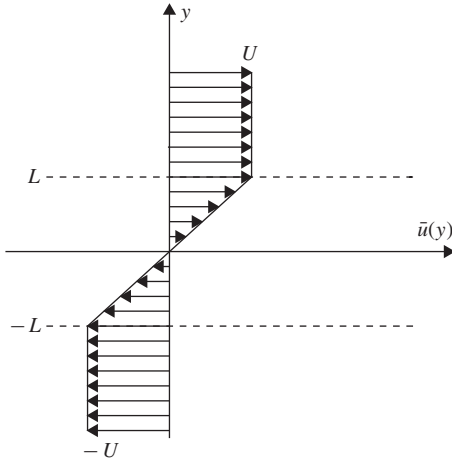
FIGURE 10.2 An idealized shear-flow profile that lends itself to analytic treatment. This profile meets both necessary conditions for instability and is found to be unstable to long waves.

$$-L < y < +L: \quad \bar{u} = \frac{U}{L}\, y, \quad \frac{d\bar{u}}{dy} = \frac{U}{L}, \quad \frac{d^2\bar{u}}{dy^2} = 0 \qquad (10.31)$$

$$+L < y: \quad \bar{u} = +U, \quad \frac{d\bar{u}}{dy} = 0, \quad \frac{d^2\bar{u}}{dy^2} = 0, \qquad (10.32)$$

where U is a positive constant, and the domain width is now infinity. Although the second derivative vanishes within each of the three segments of the domain, it is nonzero at their junctions. As y increases, the first derivative $d\bar{u}/dy$ changes from zero to a positive value and back to zero, so it can be said that the second derivative is positive at the first junction ($y = -L$) and negative at the second ($y = +L$). Thus, $d^2\bar{u}/dy^2$ changes sign in the domain, and this satisfies the first condition for the existence of instabilities. The second condition, that expression (10.17), now reduced to

$$-\bar{u}\, \frac{d^2\bar{u}}{dy^2},$$

be positive in some portion of the domain, is also satisfied because $d^2\bar{u}/dy^2$ has the sign opposite to $\bar{u}$ at each junction of the profile. Thus, the necessary conditions for instability are met, and although instabilities are not guaranteed to exist, we ought to expect them.

We now proceed with the solution. In each of the three domain segments, governing Eq. (10.9) reduces to

$$\frac{d^2\phi}{dy^2} - k^2\, \phi = 0, \qquad (10.33)$$

and admits solutions of the type $\exp(+ky)$ and $\exp(-ky)$. This introduces two constants of integration per domain segment, for a total of six. Six conditions

are then applied. First, ϕ is required to vanish at large distances:

$$\phi(-\infty) = \phi(+\infty) = 0.$$

Next, continuity of the meridional displacements at $y = \pm L$ requires, by virtue of Eq. (10.19) and by virtue of the continuity of the $\bar{u}(y)$ profile, that ϕ, too, be continuous there:

$$\phi(-L-\epsilon) = \phi(-L+\epsilon) \quad \text{and} \quad \phi(+L-\epsilon) = \phi(+L+\epsilon),$$

for arbitrarily small values of ϵ. Finally, the integration of governing equation (10.9) across the lines joining the domain segments

$$\int_{\pm L-\epsilon}^{\pm L+\epsilon} \left[(\bar{u}-c) \frac{d^2\phi}{dy^2} - k^2 (\bar{u}-c) \phi - \frac{d^2\bar{u}}{dy^2} \phi \right] dy = 0,$$

followed by an integration by parts, implies that

$$(\bar{u}-c) \frac{d\phi}{dy} - \frac{d\bar{u}}{dy} \phi$$

must be continuous at both $y = -L$ and $y = +L$. An alternative way of obtaining this result is to integrate Eq. (10.19), which is in conservative form, across a discontinuity.

Applying these six conditions leads to a homogeneous system of equations for the six constants of integration. Nonzero perturbations exist when this system admits a nontrivial solution—that is, when its determinant vanishes. Some tedious algebra yields

$$\frac{c^2}{U^2} = \frac{(1-2kL)^2 - e^{-4kL}}{(2kL)^2}. \tag{10.34}$$

Equation (10.34) is the dispersion relation, providing the wave velocity c in terms of the wavenumber k and the flow parameters L and U. It yields a unique and real c^2, either positive or negative. If it is positive, c is real and the perturbation behaves as a non-amplifying wave. But, if c^2 is negative, c is imaginary and one of the two solutions yields an exponentially growing mode [a proportional to $\exp(kc_i t)$]. Obviously, the instability threshold is $c^2 = 0$, in which case the dispersion relation (10.34) yields $kL = 0.639$. There thus exists a critical wavenumber $k = 0.639/L$ or critical wavelength $2\pi/k = 9.829L$ separating stable from unstable waves (Fig. 10.3). It can be shown by inspection of the same dispersion relation that shorter waves ($kL > 0.639$) travel without growth (because $c_i = 0$), whereas longer waves ($kL < 0.639$) grow exponentially without propagation (because $c_r = 0$). In sum, the basic shear flow is unstable to long-wave disturbances.
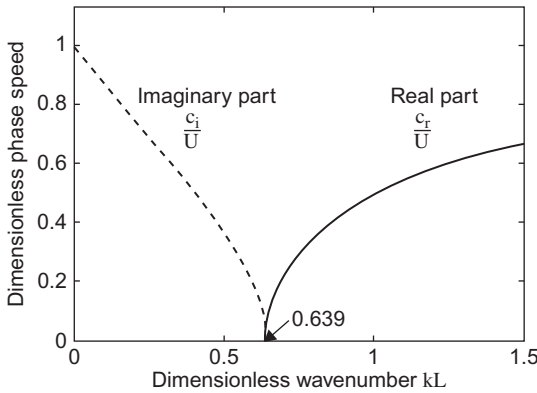
FIGURE 10.3 Plot of the dispersion relation (10.34) for waves riding on the shear flow depicted in Fig. 10.2. The lower wavenumbers k for which c_i is nonzero correspond to growing waves.

An interesting quest is the search for the fastest growing wave because this is the dominant wave, at least until finite-amplitude effects become important and the preceding theory loses its validity. For this, we look for the value of kL that maximizes kc_i, where c_i is the positive imaginary root of Eq. (10.34). The answer is $kL = 0.398$, from which follows the wavelength of the fastest growing mode:

$$\lambda_{\text{fastest growth}} = \frac{2\pi}{k} = 15.77\, L = 7.89\,(2L). \tag{10.35}$$

This means that the wavelength of the perturbation that dominates the early stage of instability is about eight times the width of the shear zone. Its growth rate is

$$(kc_i)_{\text{max}} = 0.201\,\frac{U}{L}, \tag{10.36}$$

corresponding to $c_i = 0.505U$. It is left to the reader as an exercise to verify the preceding numerical values.

At this point, it is instructive to unravel the physical mechanism responsible for the growth of long-wave disturbances. Figure 10.4 displays the basic flow field, on which is superimposed a wavy disturbance. The phase shift between the two lines of discontinuity is that propitious to wave amplification. As the middle fluid, endowed with clockwise vorticity, intrudes in either neighboring strip where the vorticity is nonexistent, it produces local vorticity anomalies, which can be viewed as vortices. These vortices generate clockwise rotating flows in their vicinity, and if the wavelength is sufficiently long, the interval between the two lines of discontinuity appears relatively short and the vortices from each side interact with those on the other side. Under a proper phase difference, such as the one depicted in Fig. 10.4, the vortices entrain one another further into the regions of no vorticity, thereby amplifying the crests and troughs of the wave. The wave amplifies, and the basic shear flow cannot persist. As the wave grows, nonlinear terms are no longer negligible, and some level of saturation is
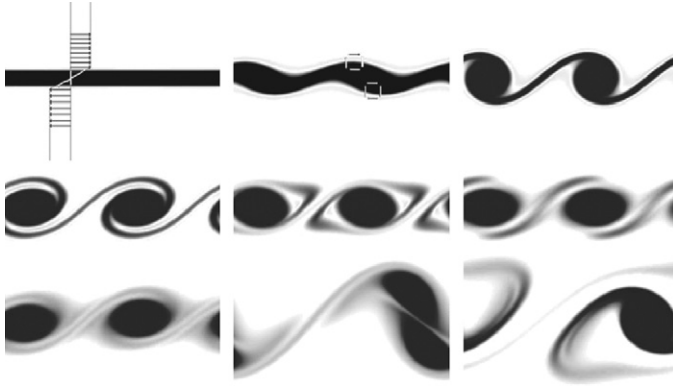
FIGURE 10.4 Finite-amplitude development of the instability of the shear flow depicted in Fig. 10.2. The troughs and crests of the wave induce a vortex field, which, in turn, amplifies those troughs and crests. The wave does not travel but amplifies with time. (The sequence of figures shown here were generated with `shearedflow.m` developed in Chapter 16.)

reached. The ultimate state (Fig. 10.4) is that of a series of clockwise vortices embedded in a weakened ambient shear flow (Dritschel, 1989; Zabusky, Hughes & Roberts, 1979).

Lindzen (1988) offers an alternative mechanism for the instability based on the fact that there are two special locations across the system. The first is the critical level y_c, where the wave speed matches the velocity of the basic flow $[c_r = \bar{u}(y_c)]$ and the other is y_0, where the vorticity of the basic flow reaches an extremum [where expression (10.14) changes sign]. A wave traveling in the direction of y_0 to y_c undergoes overreflection, that is, on entering the $[y_0, y_c]$ interval, it is being reflected toward its region of origin with a greater amplitude than on arrival. If there is a boundary or other place where the wave can be (simply) reflected, then it returns toward the region of overreflection, and on it goes. The successive overreflections of the echoing wave lead to exponential growth.

10.5   NONLINEARITIES

From Section 10.2, we note that the nonlinear advection term is responsible for the instability of the basic flow $\bar{u}(y)$. We analyzed the stability by linearizing the equations around the steady-state solution and replaced terms such as $u\partial u/\partial x$ by $\bar{u}\partial u'/\partial x$ and this led to linear equations and wave-like solutions, yet retaining the advection by the basic current $\bar{u}$. When instability occurs, the velocity perturbations grow in time, and after an initial phase during which linearization holds, they eventually reach such an intensity that $u'\partial u'/\partial x$ may no longer be neglected. We enter a nonlinear regime requiring numerical simulation. In an inviscid problem such as the present one, we then face a serious problem,

already mentioned in the Introduction, namely the aliasing of short waves into longer waves.

As shown in Section 1.12 for time series, sampling (read: discretization) sets some limits on the frequencies that can be resolved. In space instead of time, the same analysis applies, and waves of wavenumbers k_x and $k_x + 2\pi/\Delta x$ cannot be distinguished from each other in a discretization with space interval Δx. If a wavenumber k_x larger than $\pi/\Delta x$ exists, it is mistaken by the discretization as being of smaller wavenumber $k_x - 2\pi/\Delta x$ or $2\pi/\Delta x - k_x$. This misinterpretation of too rapidly varying waves can be depicted (Fig. 10.5) as a reflection of the wavenumber about the cutoff value $\pi/\Delta x$. Any wave can be decomposed in its spectral components, and let us suppose that the spectrum of a set waves (wave packet) takes the form shown in Fig. 10.6. Since waves of higher wavenumbers are reflected around the cutoff wavenumber into the resolved range, the associated spectral energy will also be transferred from the shorter unresolved waves to the longer resolved waves. If the energy level decreases with decreasing wavenumber, the spectrum alteration will be strongest near the cutoff value. In other words, the energy content of marginally resolved waves is the one most influenced by aliasing, and the manifestation is an unwanted excess of energy among barely resolved waves. This is one reason why model results ought generally to viewed as suspect at scales comparable to the grid spacing. But there is more to the problem.

The aliasing problem is particularly irksome when nonlinear advection comes into play because the quadratic term in the equation creates wave harmonics: If the velocity field is resulting from the superposition of two waves, one of wavenumber k_1 and another of wavenumber k_2 of equal amplitude and phase,

$$u = u_1 + u_2 \quad \text{with} \quad u_1 = A\,e^{ik_1 x} \quad \text{and} \quad u_2 = A\,e^{ik_2 x}, \qquad (10.37)$$

then the advection term $u\,\partial u/\partial x$ generates a contribution of the form

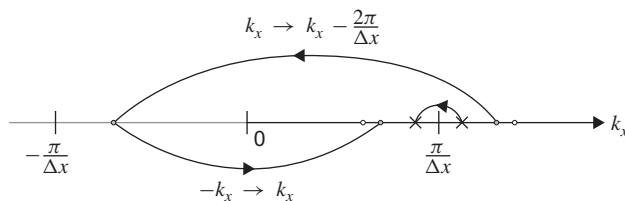$$A^2 i\,(k_1 + k_2)e^{i(k_1 + k_2)x} \qquad (10.38)$$

FIGURE 10.5 Transformation of a unresolved short wave of wavenumber $k_x > \pi/\Delta x$ into a resolved wavenumber $|k_x - 2\pi/\Delta x|$, corresponding to a reflection of wavenumber about the cutoff value $\pi/\Delta x$ as indicated for three particular values of the wavenumber identified by an open circle, a cross, and a gray dot to the right of $\pi/\Delta x$ and the wavenumbers into which they are aliased (all to the left of $\pi/\Delta x$).
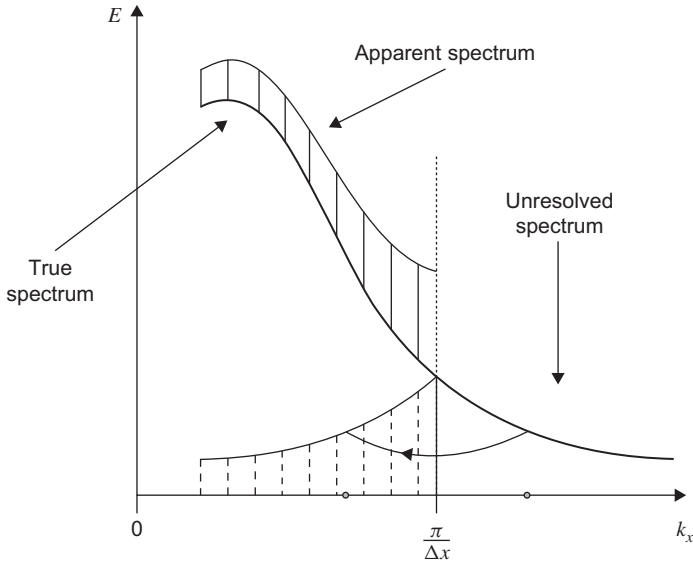
FIGURE 10.6   Spectrum alteration by aliasing, which effectively folds the numerically unresolved part of the spectrum ($k_x \geq \pi/\Delta x$) into resolved scales. The steeper the energy spectrum decrease around the cutoff wavenumber, the less aliasing is a problem. The spectrum alteration is then limited to the vicinity of the shortest resolved waves.

which introduces a new spectral component of higher wavenumber $k_1 + k_2$. Even if the two original waves are resolved by the grid, the newly created and shorter wave may be aliased and mistaken for a longer wave. This happens when $k_1 + k_2 > \pi/\Delta x$. The nonlinear advection thus creates an aliasing problem, which can seriously handicap calculations, especially if the aliasing is such that the newly created waves have a wavenumber identical to one of the original waves, k_1 for example. In this case, we have a feedback loop in which component u_1 interacts with another one and, instead of generating a shorter wave as it ought, increases its own amplitude. The process is self-repeating, and before long, the amplitude of the self-amplifying wave will reach an untolerable level. This is known as *nonlinear numerical instability*, which was first identified by Phillips (1956).

Such a self-amplification occurs when the interaction of k_1 and k_2 satisfies the aliasing condition and the new wave is aliased back into one of the original wavenumbers (here k_1):

$$(k_1 + k_2) \geq \frac{\pi}{\Delta x} \quad \text{and} \quad \frac{2\pi}{\Delta x} - (k_1 + k_2) = k_1. \tag{10.39}$$

To avoid such a situation for any wavenumber resolved by the grid (i.e., for all admissible values for k_2 varying between 0 and $\pi/\Delta x$), k_1 should not be allowed

to take values in the interval $\pi/(2\Delta x)$ to $\pi/\Delta x$. This requirement is a little bit too strong since if k_1 is not allowed to exceed $\pi/(2\Delta x)$, k_2, too, should not be allowed to do so. The highest permitted value for either k_1 or k_2 is then found by letting $k_1 = k_2$ in (10.39), and this yields $k_{max} = 2\pi/(3\Delta x)$. In other words, if we are able to avoid all waves of wavelength shorter than $2\pi/k_{max} = 3\Delta x$, nonlinear instability by aliasing can be prevented. However, disallowing these waves from the initial condition is not enough because sooner or later, they will be generated by nonlinear interaction among the longer waves. The remedy is to eliminate the shorter waves as they are being generated, and this is accomplished by *filtering*.

Filtering is a form of dissipation that mimics physical dissipation but is designed to remove preferentially the undesirable waves, that is, only those on the shortest scales resolved by the numerical grid. This can be accomplished by the filters discussed in the following section. Other methods to address aliasing and nonlinear numerical instability related to the advection term will be encountered later in Section 16.7. Before concluding this chapter, we will also describe an entirely different approach, which avoids aliasing altogether by not using a grid at all. This method, known as *contour dynamics*, follows fluid parcels along their path of motion, thus absorbing the advection terms in the material time derivative.

10.6   FILTERING

We saw earlier that the leapfrog method generates spurious modes (flip-flop in time), and we just realized that spatial modes near the $2\Delta x$ cutoff ("saw-tooth" structure in space) are poorly reproduced and prone to aliasing. We further showed how nonlinearities can create aliasing problems around the $2\Delta x$ mode. Naturally, we would now like to remove these unwanted oscillations from the numerical solution. For the spatial saw-tooth structure, we already have at our disposal a method for eliminating shorter waves: physical diffusion. However, physical diffusion in the model may not always be sufficient to suppress or even control the $2\Delta x$ mode, and additional dissipation, of a numerical nature, becomes necessary. This is called *filtering*.

In this section, we concentrate on explicit filtering, designed to damp short waves. Let us start with a discrete filter inspired by the physical diffusion operator:

$$\widehat{c}_i^{\,n} = \tilde{c}_i^{\,n} + \varkappa \underbrace{\left(\tilde{c}_{i+1}^{\,n} - 2\tilde{c}_i^{\,n} + \tilde{c}_{i-1}^{\,n} \right)}_{\simeq \Delta x^2 \frac{\partial^2 c}{\partial x^2}}, \tag{10.40}$$

in which the new (filtered) value $\widehat{c}_i^{\,n}$ is henceforth replacing the original (unfiltered) value $\tilde{c}_i^{\,n}$. The preceding formulation is equivalent to introducing a diffusion term with diffusivity $\varkappa \Delta x^2/\Delta t$, which enhances physical diffusion, if any.

The behavior of this filter can be analyzed with the aid of Fourier modes $[\exp(ik_x i\Delta x)]$, thus providing the "amplification" factor, which in this case is actually a damping factor:

$$\varrho = 1 - 4\varkappa \sin^2\left(\frac{k_x \Delta x}{2}\right). \tag{10.41}$$

For well-resolved waves, the amplification factor is close to unity (no change of amplitude), whereas for the $2\Delta x$ wave ($k_x = 2\pi/2\Delta x$), its value is $1-4\varkappa$. The value $\varkappa = 1/4$ therefore eliminates the shortest wave in a single pass of the filter, but intermediate wavelengths are partially reduced, too, and a smaller value of $\varkappa$ is generally used in order not to dampen unnecessarily the intermediate scales of the solution. Therefore, a compromise needs to be reached between our desire to eliminate the $2\Delta x$ component while least affecting the rest of the solution.

To alleviate such compromise, more selective filters can be implemented. These are of the biharmonic type and require a wider stencil (more grid points). For example,

$$\widehat{c}_i^n = \tilde{c}_i^n + \frac{\varkappa}{4}\underbrace{\left(-\tilde{c}_{i+2}^n + 4\tilde{c}_{i-1}^n - 6\tilde{c}_i^n + 4\tilde{c}_{i+1}^n - \tilde{c}_{i+2}^n\right)}_{\simeq -\Delta x^4 \frac{\partial^4 \tilde{c}}{\partial x^4}} \tag{10.42}$$

leads to the more scale-selective damping factor

$$\varrho = 1 - \varkappa\left[4\sin^2\left(\frac{k_x \Delta x}{2}\right) - \sin^2\left(\frac{2k_x \Delta x}{2}\right)\right]. \tag{10.43}$$

The difference in the case $\varkappa = 1/4$ is illustrated in Fig. 10.7. Both diffusion-like and biharmonic filters [Eqs. (10.40) and (10.42), respectively] eliminate the $2\Delta x$ mode with the same value of $\varkappa$. Figure 10.7 also shows that components of intermediate scales are less affected by the biharmonic filter than by the diffusion-like filter. However, the biharmonic filter may introduce nonmonotonic behavior because there are negative coefficients in its stencil (10.42).

As for the diffusion-like filter, the biharmonic filter is sometimes made explicit in the undiscretized model equations by an additional term of the form $-\mathcal{B}\partial^4 \tilde{c}/\partial x^4$, with $\mathcal{B} = \varkappa \Delta x^4/(4\Delta t)$. The approach can, of course, be extended to ever larger stencils with increased scale selectivity but at the cost of additional computations.

It should be noted that the coefficients used in the filters are depending on the grid spacing and time step, whereas physical parameters do not, unless they parameterize subgrid-scale effects. In the latter case, the grid size can be involved in the parameterization, as seen in Section 4.2. However, we should not confuse the different concepts: The physical molecular diffusion, the standard
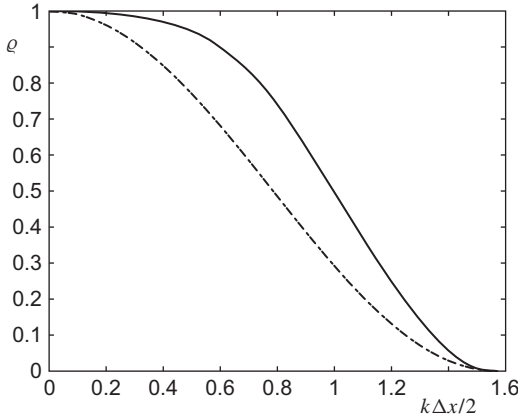
FIGURE 10.7 Damping factor as a function of wavelength for two different filters: regular diffusion [Eq. (10.40), dashed-dotted line] and biharmonic operator [Eq. (10.42), solid line], each for $\varkappa = 1/4$. Both filters eliminate the $2\Delta x$ mode completely ($\varrho = 0$), but the biharmonic filter is more scale selective in the sense that it damps less the intermediate-scale components (ϱ closer to unity for these).

microturbulent (eddy) diffusion, subgrid-scale diffusion introduced to parameterize mixing at scales longer than turbulent motions yet shorter than the grid spacing, diffusion associated with explicit filtering (the subject of the present section), and finally, numerical diffusion caused by the numerical scheme (totally uncoded). It is unfortunately not always clearly stated in model applications which type of diffusion is being meant when the authors mention their model's diffusion parameters.

For filtering in time, we can adopt the same filtering technique. Because the spatial filter replaces the model values by a filtered version obtained via Eq. (10.40), one way of eliminating the flip-flop mode is

$$\widehat{c}^{\,n} = \tilde{c}^{\,n} + \varkappa \left(\tilde{c}^{\,n+1} - 2\tilde{c}^{\,n} + \tilde{c}^{\,n-1} \right). \tag{10.44}$$

However, this is not very practical since it requires that past values of $\tilde{c}$ be stored for later filtering. Note also how filtering at time level n must wait until values have been computed at time level $n+1$. This does not avoid the nonlinear interactions of the spurious mode with the physical modes. It is better, therefore, to blend the filtering with time stepping and replace the unfiltered solution by the filtered one as soon as it becomes available. Suppose for example that we have a new value of $\tilde{c}^{\,n+1}$ obtained with the leapfrog scheme,

$$\tilde{c}^{\,n+1} = \widehat{c}^{\,n-1} + 2\Delta t \, Q\left(t, \tilde{c}^{\,n} \right), \tag{10.45}$$

with the usual source term Q regrouping all spatial operators. We can then filter $\tilde{c}^{\,n}$ with

$$\widehat{c}^{\,n} = \tilde{c}^{\,n} + \varkappa \left(\tilde{c}^{\,n+1} - 2\tilde{c}^{\,n} + \widehat{c}^{\,n-1} \right), \tag{10.46}$$

and immediately store it in the array holding $\tilde{c}^n$. Note how $\widehat{c}^{n-1}$ appears in the filtering and leapfrog step instead of $\tilde{c}^{n-1}$ because the filtered value has already superseded the original one. This filter, known as the *Asselin filter* (Asselin, 1972), is commonly used in models with leapfrog time discretization. In order not to filter excessively, small values of $\varkappa$ can be used. Alternatively, the filter can be applied only intermittently or with varying intensity $\varkappa$.

More selective filters in time can be inspired by the spatial filter (10.42), but these would require the storage of additional intermediate values of the state vector because the filter involves more time levels (five in the biharmonic case), while the leapfrog scheme requires that only three levels be stored.

Other filters exist, some of them based on intermittent re-initialization of the leapfrog time integration by simple Euler steps, but all of them should be applied with caution because they always filter part of the physical solution or alter the truncation error.

10.7   CONTOUR DYNAMICS

The preceding stability analysis and aliasing problem gives us a nice opportunity to introduce yet another numerical method, the family of so-called boundary element methods. This method was first applied to vortex calculations by Norman Zabusky[2] (Zabusky et al., 1979). To illustrate the approach, we start from the simple task of retrieving the velocity field from a known vorticity distribution in two dimensions. The vorticity ω is related to the velocity components u and v by

$$\frac{\partial v}{\partial x} - \frac{\partial u}{\partial y} = \omega, \tag{10.47}$$

and it follows by inversion of this definition that the velocity accompanying a localized vortex patch of area ds and uniform vorticity ω in the absence of boundary conditions (i.e., for an infinite domain) is given by

$$2\pi r \, dv_\theta = \omega \, ds, \tag{10.48}$$

where $r = \sqrt{(x-x')^2 + (y-y')^2}$, and v_θ is the velocity component perpendicular to the line joining the vortex patch to the point under consideration (left side of Fig. 10.8). The result follows from a straightforward application of Stokes theorem, which states that the circulation of the velocity along a contour (here circle of radius r), that is $2\pi r \, dv_\theta$, is equal to the integration of the vorticity within that contour (here ωds).

---

[2]See his biography at the end of this chapter.

In vectorial notation, the infinitesimal velocity associated with a differential patch ds of vorticity ω is

$$d\mathbf{u} = \frac{\omega}{2\pi r} \frac{\mathbf{k} \times (\mathbf{x} - \mathbf{x}')}{r} \, ds, \tag{10.49}$$

which can be integrated over space for a nonuniform distribution $\omega(x, y)$ over a finite area (right side of Fig. 10.8). We obtain

$$\mathbf{u}(x, y) = \frac{1}{2\pi} \int \int \omega(x', y') \frac{\mathbf{k} \times (\mathbf{x} - \mathbf{x}')}{r^2} \, dx' \, dy'. \tag{10.50}$$

This provides the velocity field as a function of the vorticity distribution, up to an irrotational velocity field. In an infinite domain (i.e., with no boundary conditions), the latter is zero. Suppose for now that we have a single patch of constant vorticity so that

$$u(x, y) = \frac{\omega}{2\pi} \int \int \frac{-(y - y')}{(x - x')^2 + (y - y')^2} \, dx' \, dy' \tag{10.51a}$$

$$v(x, y) = \frac{\omega}{2\pi} \int \int \frac{(x - x')}{(x - x')^2 + (y - y')^2} \, dx' \, dy', \tag{10.51b}$$

where the integral is performed over the vorticity patch delimited by its contour $\mathcal{C}$ (Fig. 10.8). Noting that integrands are derivatives of the function

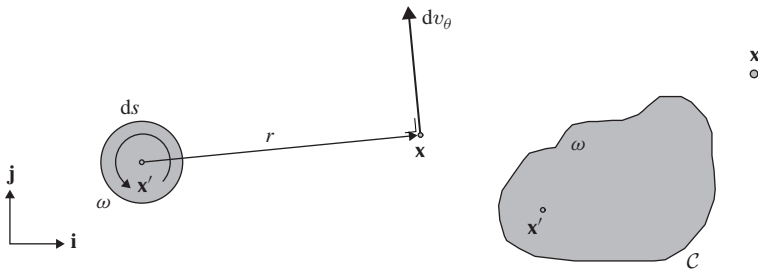$$\phi = \ln \left[\frac{(x - x')^2 + (y - y')^2}{L^2} \right], \tag{10.52}$$

FIGURE 10.8   Element dv_θ of velocity associated with an infinitesimal vortex patch of area ds and vorticity ω (left panel). Integration over a finite patch of nonzero vorticity within contour $\mathcal{C}$ gives the associate velocity field (right panel). Note that the domain is infinitely wide outside the vortex patch.

we can rewrite the velocity components as

$$u(x, y) = \frac{\omega}{4\pi} \int \int \frac{\partial \phi}{\partial y'} \, dx' \, dy' = -\frac{\omega}{4\pi} \oint_{\mathcal{C}} \phi \, dx' \tag{10.53a}$$

$$v(x, y) = \frac{\omega}{4\pi} \int \int -\frac{\partial \phi}{\partial x'} \, dx' \, dy' = -\frac{\omega}{4\pi} \oint_{\mathcal{C}} \phi \, dy', \tag{10.53b}$$

for which we performed integration by parts to reduce the integral over the area of nonzero vorticity to a line integral along its perimeter. The symbol $\oint$ means that the integral is taken as x' and y' vary along the closed perimeter $\mathcal{C}$ with the patch on the left. Thus, we can express the velocity vector $\mathbf{u}$ at any point due to a patch of uniform vorticity ω as

$$\mathbf{u}(x, y) = -\frac{\omega}{4\pi} \oint_{\mathcal{C}} \ln\left[\frac{(x-x')^2 + (y-y')^2}{L^2} \right] dx'. \tag{10.54}$$

When several vorticity patches are present, all we have to do is to add the contributions of the different patches. However, there is a slight difficulty when a patch is contained within another one. For example, in Fig. 10.9, the ω_3 vorticity lies entirely within the ω_2 vorticity patch. For the ω_2 patch, the contour integration breaks into two parts, one for the outer contour $\mathcal{C}_2$ traveled counterclockwise (with vorticity ω_2 to its left) and the other for the inner contour $\mathcal{C}_3$ traveled clockwise (again with vorticity ω_2 to its left). The latter contour integral needs to be repeated for the ω_3 patch, this time traveled counterclockwise and with ω_3 in its integrand. The addition of the last two integrals leads to a single integration along $\mathcal{C}_3$ performed counterclockwise with the vorticity jump $\delta\omega_3 = \omega_3 - \omega_2$ in its integrand. For any number of contours, we have

$$\mathbf{u}(x, y) = -\frac{1}{4\pi} \sum_m \delta\omega_m \oint_{\mathcal{C}_m} \ln\left[\frac{(x-x')^2 + (y-y')^2}{L^2} \right] dx', \tag{10.55}$$

where the sum is performed over all existing contours, and where $\delta\omega_m$ is the vorticity jump across contour $\mathcal{C}_m$ (inside value minus outside value).

Up to here we only established a diagnostic tool to retrieve the velocity field from a given distribution of vorticity patches. To predict the evolution of these patches, we now have to solve the governing equation for vorticity. In the absence of friction or any other vorticity-altering process, vorticity is conserved and simply advected by the flow. Thus, points within a given vortex patch will retain their vorticity and remain within their original patch. All we have to do is to predict the evolution of the *boundary* of each patch, that is, the contours, hence the name *contour dynamics* given to the method.

Points along the contours are physical fluid points and therefore move with the local flow velocity, that is, the velocity field of Eq. (10.55) taken at contour points. In practice, such integration can rarely be performed analytically, and numerical methods must be devised. The most natural discretization consists of dividing all contours into segments (Fig. 10.10), and the contour integrals then
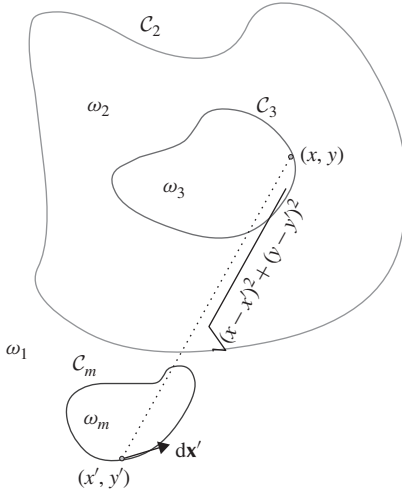
FIGURE 10.9 When several contours are involved in the velocity determination, contour integrals must be added to one another, and the relevant quantity along a contour is the vorticity jump across it. For the case depicted here, it is $\omega_3 - \omega_2$ for contour $\mathcal{C}_3$.
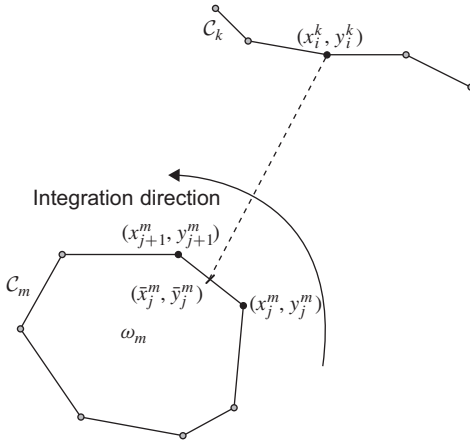

FIGURE 10.10 Discretization of contour integrals achieved by using a mid-point evaluation of the integrand along the mth contour at location $((x_j^m + x_{j+1}^m)/2, (y_j^m + y_{j+1}^m)/2)$. In this way, the singularity of the logarithm is avoided when the point (x_i^k, y_i^k) for which the integral is evaluated lies on the same contour along which the integral is performed.

reduce to sums of discrete contributions. The integral discretization has to deal with a singularity when the point (x, y) for which the velocity is computed lies on the same contour as where integration takes place and eventually coincides with point (x', y'). A simple way to avoid the problem is to use a staggered approach for the integration, that is, to evaluate the integrand at mid-distance between nodes j and $j+1$ (Fig. 10.10): For point (x_i^k, y_i^k) on contour k (with k possibly equal to m) where the velocity is being calculated, the pieces of the integral on contour $\mathcal{C}_m$ are approximated as

$$I_m(x_i^k, y_i^k) = \sum_{j=1}^{N} \ln\left[\frac{(x_i^k - \bar{x}_j^m)^2 + (y_i^k - \bar{y}_j^m)^2}{L^2}\right] \left(x_{j+1}^m - x_j^m\right) \qquad (10.56a)$$

$$J_m(x_i^k, y_i^k) = \sum_{j=1}^{N} \ln\left[\frac{(x_i^k - \bar{x}_j^m)^2 + (y_i^k - \bar{y}_j^m)^2}{L^2}\right] \left(y_{j+1}^m - y_j^m\right) \qquad (10.56b)$$

$$\text{with} \quad \bar{x}_j^m = \frac{x_{j+1}^m + x_j^m}{2}, \quad \bar{y}_j^m = \frac{y_{j+1}^m + y_j^m}{2}, \qquad (10.57)$$

where the sum covers the N segments[3] of the mth contour. To close the contour, we define for convenience $x_{N+1}^m = x_1$ and $y_{N+1}^m = y_1$. Note that there is no singularity because when m takes its turn to equal k and j takes its turn to equal i, the expression inside the logarithm remains nonzero. Finally, once individual integrals are calculated, the velocity components can be obtained by summing over all contour integrals:

$$u(x_i^k, y_i^k) = -\frac{1}{4\pi} \sum_m \delta\omega_m \, I_m\left(x_i^k, y_i^k\right)$$

$$v(x_i^k, y_i^k) = -\frac{1}{4\pi} \sum_m \delta\omega_m \, J_m\left(x_i^k, y_i^k\right),$$

and every node i on every contour k can be moved in time with the velocity:

$$\frac{dx_i^k}{dt} = u\left(x_i^k, y_i^k\right) \qquad (10.58a)$$

$$\frac{dy_i^k}{dt} = v\left(x_i^k, y_i^k\right). \qquad (10.58b)$$

The time integration can be performed by any method presented in Chapter 2. The Lagrangian (i.e., fluid following) displacements lead to deformation of the contours (see also Lagrangian approach of Section 12.8).

The simple numerical integration method outlined here is easily implemented (see, e.g., contourdyn.m). To try the method, we simulate the evolution of a narrow band of uniform vorticity (Fig. 10.11). Except for the curvature, this case is that of the shear layer instability seen in Section 10.4. Note the growing instabilities of the shear layer manifested as rolling waves.
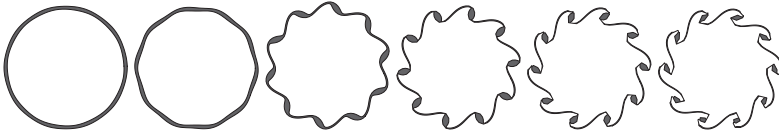

FIGURE 10.11 Evolution of a narrow band of uniform vorticity simulated with contour dynamics.

---

[3]The number of segments per contour can, of course, be different for each contour, in which case $N = N_m$.
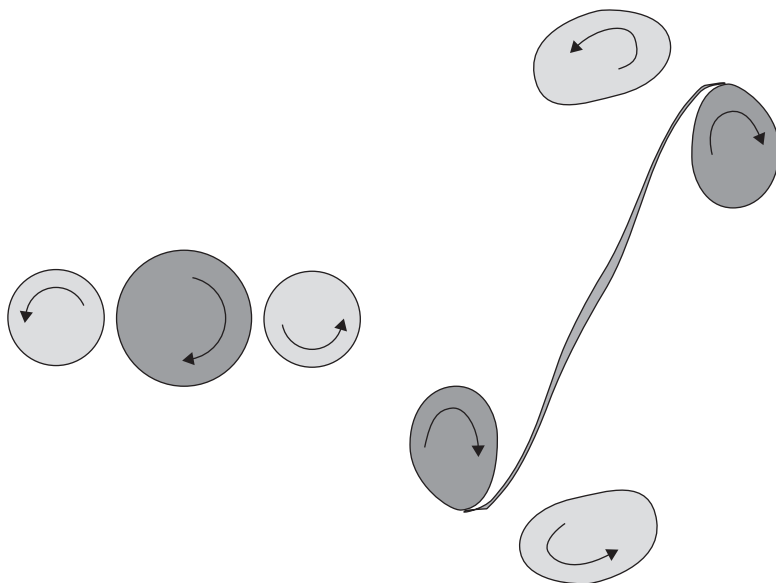
FIGURE 10.12   Two positive vorticity patches flanking a middle vortex of opposite vorticity and twice the area (left panel). Depending on the distances between the initial vortices, several outcomes are possible. One of them is vortex breakup and creation of vortex pairs (right panel).

The method can also be used to study the evolution and interaction of inviscid vortex patches in an infinite domain (Fig. 10.12), with the distinct advantage that no aliasing is present and that, in principle, no numerical dissipation needs to be added to stabilize the nonlinear advection. In reality, some dissipation is necessary because tearing and shearing of the eddies can generate filaments that become ever thinner, yet never disappear when there is no viscosity. Because the integration along one side of a thin filament almost nearly cancels that along the other side, the model makes unnecessary calculations, and it would be best if filaments could be severed.

Because the discretization uses only a finite number of fluid parcels on each contour, the contours cannot be tracked down to their shortest scales, and some special treatment becomes necessary when adjacent points are getting too close in some places and too distant in other places. Removing crowded points and inserting new ones in sparse areas is required. Procedures dealing with these problems are properly called *contour surgery* and have been optimized by Dritschel (1988). This eliminates some of the smallest structures and amounts to numerical dissipation.

To conclude the section, we observe that the method of contour dynamics cleverly replaces a two-dimensional problem of Eulerian vorticity evolution (i.e., on a 2D fixed array of points) with the problem of moving one-dimensional contours in a Lagrangian way (i.e., with points following the fluid). This reduces

the complexity of the problem, but we must realize that the numerical cost of the methods is still proportional to M^2N^2 for M contours of N segments, since for each of the MN discrete points, a sum over all other points must be performed. However, because of the one-dimensional distribution of the unknowns, resolution is increased compared to an Eulerian model in which a Poisson equation must be solved in two dimensions (see Section 16.7). The reduction of complexity is possible only because we exploited the fact that there are no boundary conditions and that vorticity remains constant between contours. To decrease further the number of computations, it can be noticed that the integrals are dominated by the contributions near the singularities. Hence, the contributions of points far away from singularities can be treated in a less precise manner without penalizing the overall accuracy. One way to do so is to group them. Such simplifications can bring the computational cost down to $MN \log(MN)$ operations (e.g., Vosbeek, Clercx & Mattheij, 2000). The accuracy of the numerical integration can also be enhanced by fitting a high-order analytical function to the contour points near singularities and then integrating the resulting integrand exactly.

For a continuous vorticity distribution without boundaries, we can still apply the approach by breaking the continuous vorticity into discrete vorticity levels (see Numerical Exercise 10.5). Generalization to stratified systems and more complicated governing equations is also possible (e.g., Mohebalhojeh & Dritschel, 2004).

ANALYTICAL PROBLEMS

10.1. Show that the variable a introduced in Eq. (10.18) is the amplitude of the meridional displacement, as claimed in the footnote.

10.2. What can you say of the stability properties of the following flow fields on the f-plane?

$$\bar{u}(y) = U\left(1 - \frac{y^2}{L^2}\right) \quad (-L \leq y \leq +L) \tag{10.59}$$

$$\bar{u}(y) = U \sin\frac{\pi y}{L} \quad (0 \leq y \leq L) \tag{10.60}$$

$$\bar{u}(y) = U \cos\frac{\pi y}{L} \quad (0 \leq y \leq L) \tag{10.61}$$

$$\bar{u}(y) = U \tanh\left(\frac{y}{L}\right) \quad (-\infty < y < +\infty). \tag{10.62}$$

10.3. A zonal shear flow with velocity profile

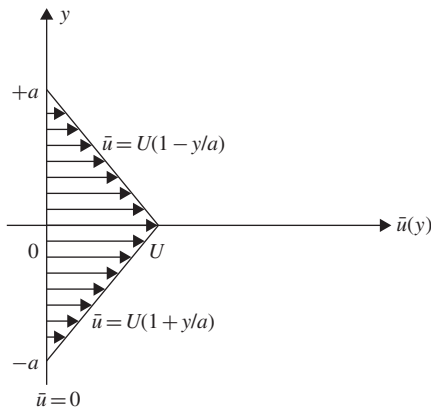$$\bar{u}(y) = U\left(\frac{y}{L} - 3\frac{y^3}{L^3}\right)$$

FIGURE 10.13   A jet-like profile (for Analytical Problem 10.6).

occupies the channel $-L \le y \le +L$ on the beta plane. Show that if $|U|$ is less than $\beta_0 L^2/12$, this flow is stable.

10.4. The atmospheric jet stream is a wandering zonal flow of the upper troposphere, which plays a central role in midlatitude weather. If we ignore the variations in air density, we can model the average jet stream as a purely zonal flow, independent of height and varying meridionally according to

$$\bar{u}(y) = U \exp\left(-\frac{y^2}{2L^2}\right),$$

in which the constants U and L, characteristics of the speed and width, are taken as 40 m/s and 570 km, respectively. The jet center ($y=0$) is at 45°N where $\beta_0 = 1.61 \times 10^{-11}$ m^{-1}s^{-1}. Is the jet stream unstable to zonally propagating waves?

10.5. Verify the semicircle theorem for the particular shear flow studied in Section 10.4. In other words, prove that $|c_r| < U$ for stable waves and $c_i < U$ for unstable waves. Also, prove that the wavelength leading to the highest growth rate, kc_i, is 15.77L, as stated in the text.

10.6. Derive the dispersion relation and establish a stability threshold for the jet-like profile of Fig. 10.13.

10.7. Redo Analytical Problem 10.6 in a channel between $y=-a$ and $y=a$.

NUMERICAL EXERCISES

10.1. Redo the analysis of nonlinear aliasing for a cubic term like $du/dt = -u^3$ in the governing equation for u. Why do you think aliasing is less of a concern in this particular case?

10.2. An elliptic vortex patch with uniform vorticity inside and zero vorticity outside is called a *Kirchhoff vortex*. Use `contourdyn.m` with `itest=1` to study the evolution of Kirchhoff vortices of aspect ratios 2:1 and 4:1. What do you observe? Implement another time-integration scheme (among which the explicit Euler scheme) and analyze how it behaves with a circular eddy. (*Hint*: Love (1983) provides a stability analysis of the Kirchhoff vortex.)

10.3. Experiment with `contourdyn.m` using `itest=4` in which two identical eddies are placed at various distances. Start with `dist=1.4` and then try the value `1.1`. What happens? Which numerical parameters would you adapt to improve the numerical simulation?

10.4. Simulate the eddy separation shown in Fig. 10.12 using `contourdyn.m`.

10.5. Discretize a circular eddy with vorticity varying linearly from zero at the rim to a maximum at the center by using M different vorticity values in concentric annuli. Then simulate its evolution with $M = 3$.

10.6. Verify your findings of Analytical Problem 10.6 by adapting `sheared-flow.m` to simulate the evolution of the most unstable periodic perturbation (for details on the numerical aspects, see Section 16.7).

10.7. Adapt `shearedflow.m` to investigate the so-called Bickley jet with profile given by

$$\bar{u}(y) = U \operatorname{sech}^2\left(\frac{y}{L}\right) \quad (-\infty < y < +\infty). \quad\quad (10.63)$$

Louis Norberg Howard
1929–

Applied mathematician and fluid dynamicist, Louis Norberg Howard has made numerous contributions to hydrodynamic stability and rotating flow. His famous semicircle theorem was published in 1961 as a short note extending some contemporary work by John Miles. Howard is also well known for his theoretical and experimental studies of natural convection. With Willem Malkus, he devised a simple waterwheel model of convection that, like real convection, can exhibit resting, steady, and periodic and chaotic behaviors. Howard has been a regular lecturer at the annual Geophysical Fluid Dynamics Summer Institute at the Woods Hole Oceanographic Institution, where his audiences have been much impressed by the breadth of his knowledge and the clarity of his explanations. (*Photo credit: L. N. Howard*)

Norman Julius Zabusky
1929–

Educated as an electrical engineer, Norman Zabusky spent the early part of his career working on plasma physics, and this led him to a lifetime pursuit of fluid turbulence by computational simulation. Vorticity dynamics lie at the center of his investigations. In the mid-1980s, he invented the method of contour dynamics (presented in this chapter) to investigate with greater precision the behavior of vorticity in two-dimensional flows in the absence of viscosity. Equipped with low-dissipation three-dimensional models of turbulent flows of his own design, Zabusky has been able to document in details the complicated processes of vortex tube deformation and reconnection. He firmly believes that progress in fluid turbulence demands a mathematical understanding of nonlinear coherent structures in weakly dissipative systems. In addition, Professor Zabusky has been fascinated by artistic renditions of waves and vortices in air and water, across ages and cultures. He wrote a book titled *From Art to Modern Science: Understanding Waves and Turbulence*. (*Photo credit: Rutgers University*)